# Strong variant selection observed in the $\alpha$-$\epsilon$ martensitic transition of iron under quasihydrostatic compression along $[111]_\alpha$

Naoki Ishimatsu [1,*] Daiki Miyashita,[1] and Saori I. Kawaguchi [2]

[1]*Graduate School of Advanced Science and Engineering, Hiroshima University, 1-3-1 Kagamiyama, Higashihiroshima, Hiroshima 739-8526, Japan*

[2]*Japan Synchrotron Radiation Research Institute (JASRI), SPring-8 1-1-1 Kouto, Sayo-cho, Sayo-gun, Hyogo 679-5198 Japan*

The $\alpha$ (bcc) phase of single-crystalline iron was compressed along the $[111]_\alpha$ direction under quasihydrostatic and nonhydrostatic conditions. The emergence of the $\epsilon$ (hcp) phase variants via the pressure-induced martensitic transformation was investigated using x-ray diffraction and optical observations of the sample surface. In quasihydrostatic compression, the $\alpha$-$\epsilon$ transition occurred at approximately 14 GPa accompanied by the sudden appearance of texture structures on the mirror-polished sample surface. The texture structure divided the sample surface into two characteristic regions: distorted regions with undulations and flat regions without undulations. Although martensitic transformation based on the Burgers model allows for the emergence of 12 $\epsilon$ variants from one single-crystalline phase, the transition proceeded according to the Burgers model, but selected variants preferably emerged depending on the regions in the texture structure. The flat region consisted of only three variants whose $c$ axes were parallel to the sample surface. The region near the undulation exhibited a large number of variants whose $c$ axes aligned parallel and nonparallel to the sample surface. The $\alpha$-$\epsilon$ transition under nonhydrostatic compression deviated from the Burgers model, and the variant selection was not observed. This study demonstrates that the quasihydrostatic compression along $[111]_\alpha$ reduces the number of variants via strong variant selection. The strong preferred orientation is useful for investigating the anisotropy of physical properties in the $\epsilon$ phase.

## I. INTRODUCTION

Iron transforms from the $\alpha$ (bcc) parent phase to a $\epsilon$ (hcp) martensite phase at $\sim$14 GPa at room temperature. The $\alpha$-$\epsilon$ transition has attracted great interest since its discovery by Bancroft *et al.* in 1956 [1] because the $\epsilon$ phase of iron is an important material for both solid-state physics [2–4] and geosciences [5,6]. Single-crystalline $\epsilon$ phase iron has recently become necessary due to the increased demand in measuring the crystallographic anisotropy in electric resistivity, thermal conductivity, and elasticity of $\epsilon$-Fe [7] as the constituent structure in the earth's inner core. Single-crystalline samples are also required for comprehensive understanding of the magnetic states in the $\epsilon$ phase [8,9]. Nevertheless, not only synthesizing a single-crystalline $\epsilon$-Fe synthesis, but also obtaining a preferably oriented polycrystalline sample is still a challenge. This is because the martensitic transformation allows multiple paths to various crystal orientations of the martensite crystals, which are called variants. The martensitic transition, therefore, could easily develop a plural number of $\epsilon$ phase variants even by starting with a single-crystalline $\alpha$-Fe.

The Burgers model is an established model to interpret the $\alpha$-$\epsilon$ transition of iron. The transition, based on this model, develops via two types of reconstructive deformations as shown in Fig. 1: shear deformation and shuffle movement

[10]. Recently, the martensitic transition process was investigated thorough a local structure analysis using extended x-ray absorption fine structure, revealing that the transition was driven by the $\langle 111 \rangle_\alpha$ shear deformation [11,12]. Therefore, if anisotropic shear deformation works on the $\alpha$ phase of iron, one can expect that the variants appear selectively depending on the orientational relationship between the shear stresses and the allowed shear deformation.

The emergence of $\epsilon$ variants from single-crystalline $\alpha$ iron has been investigated by x-ray diffraction (XRD) measurements under quasihydrostatic [13] and nonhydrostatic conditions [14]. Both experiments compressed the single crystal of Fe along the $[001]_\alpha$ direction. The quasihydrostatic experiment revealed that the transition proceeded via the Burgers model with no variant selection, and all 12 variants of $\epsilon$ phase emerged with equal probabilities [13]. The absence of the variant selection is probably attributed to the unique angular relationship between the compression axis and shear deformation where the main compression $[001]_\alpha$ axis has the same angle of $54.74°$ with all four shear $\langle 111 \rangle_\alpha$ deformations. However, if a single-crystalline sample is compressed along different crystal orientations, for example, the $[111]_\alpha$ axis, one $[111]_\alpha$ shear deformation is parallel to the compression axis, whereas the other three $[\bar{1}11]_\alpha$, $[1\bar{1}1]_\alpha$, and $[11\bar{1}]_\alpha$, possess the same $70.53°$ angle with the compression axis (see Fig. 1). The main purpose of this paper is to examine the preferred variant emergence in the case of multiple relationship between the compression axis and shear deformations.

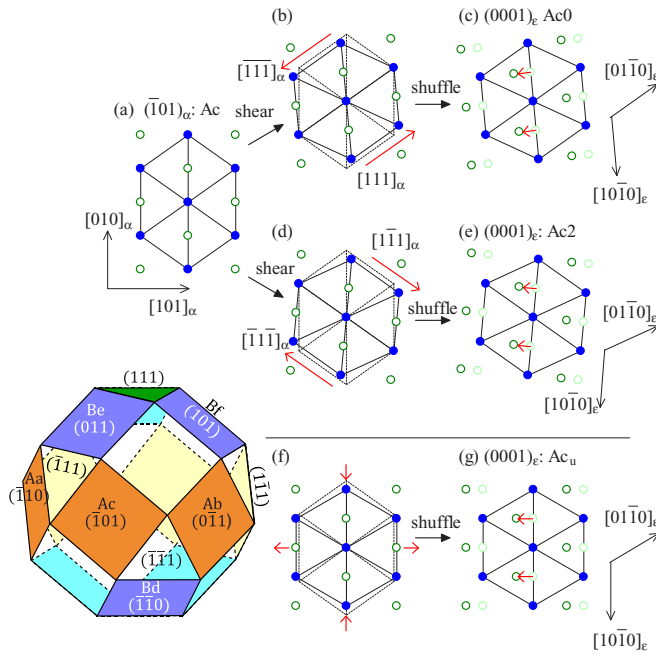---
*ishimatsunaoki@hiroshima-u.ac.jp

FIG. 1. (a)–(e) Schematic of the martensitic transition of iron based on the Burgers model. The atomic arrangement viewed from the $[10\bar{1}]_\alpha$ direction is depicted in Refs. [10,11]. The open and closed circles correspond to iron atoms on the adjacent $(\bar{1}01)_\alpha$ planes. (f) and (g) An alternative transition model via uniaxial compression and expansion along $[010]_\alpha$ and $[101]_\alpha$, respectively. The polyhedron in the left bottom inset illustrates two types ($A$ and $B$) of the $\{110\}_\alpha$ planes with respect to the vertical $[111]_\alpha$ axis.

TABLE I. The 12 possible variants introduced by the $\alpha$-$\epsilon$ transition via compression along the $[111]_\alpha$ direction and Burgers model. The symbols are used in the simulated XRD patterns.

| ID | Symbol /color | Conjugate plane $(hkl)_\alpha \parallel (0001)_\epsilon$ | Direction of shear $\pm[hkl]_\alpha$ |
|---|---|---|---|
| Aa0 | ●/black | a: $(\bar{1}10)_\alpha$ | 0: $\pm[111]_\alpha$ |
| Aa3 | ●/green | a: $(\bar{1}10)_\alpha$ | 3: $\pm[11\bar{1}]_\alpha$ |
| Ab0 | ■/black | b: $(0\bar{1}1)_\alpha$ | 0: $\pm[111]_\alpha$ |
| Ab1 | ■/red | b: $(0\bar{1}1)_\alpha$ | 1: $\pm[\bar{1}11]_\alpha$ |
| Ac0 | ◆/black | c: $(\bar{1}01)_\alpha$ | 0: $\pm[111]_\alpha$ |
| Ac2 | ◆/blue | c: $(\bar{1}01)_\alpha$ | 2: $\pm[1\bar{1}1]_\alpha$ |
| Bd2 | ○/blue | d: $(110)_\alpha$ | 2: $\pm[1\bar{1}1]_\alpha$ |
| Bd1 | ○/red | d: $(110)_\alpha$ | 1: $\pm[\bar{1}11]_\alpha$ |
| Be3 | □/green | e: $(011)_\alpha$ | 3: $\pm[11\bar{1}]_\alpha$ |
| Be2 | □/blue | e: $(011)_\alpha$ | 2: $\pm[1\bar{1}1]_\alpha$ |
| Bf1 | ◇/red | f: $(101)_\alpha$ | 1: $\pm[\bar{1}11]_\alpha$ |
| Bf3 | ◇/green | f: $(101)_\alpha$ | 3: $\pm[11\bar{1}]_\alpha$ |

This study compressed the $\alpha$ (bcc) phase of single-crystalline iron along the $[111]_\alpha$ direction, and investigated emergence of $\epsilon$ (hcp) phase variants via the martensitic transformation under quasihydrostatic and nonhydrostatic conditions by using x-ray diffraction and the optical observation of the sample surface. The quasihydrostatic compression along the $[111]_\alpha$ axis exhibited strong variant selections and reduced the number of variants down to three. This paper is organized into three experiments. The first experiment examines the validity of the Burgers model for the $[111]_\alpha$ compression under quasihydrostatic conditions (run I). The second experiment discusses the relationship between variant selection and texture structure on the sample surface (run II). The last experiment reports the deviation from the Burgers model in the case of nonhydrostatic compression using methanol:ethanol (ME) (=4:1 ratio) solutions (run III).

## II. A MODEL: BURGERS TYPE $\alpha$-$\epsilon$ TRANSITION PROCESS

Figures 1(a)–1(e) depict a schematic of the transition process via the Burgers model [10,11] viewed from the $[\bar{1}01]_\alpha \parallel [0001]_\epsilon$ direction. When the shear stress works along the $\pm[111]_\alpha$ direction, the hcp martensite phase rotates $-5.5°$ in the anticlockwise direction with respect to the parent bcc phase, whereas the martensite phase rotates $+5.5°$ in the clockwise direction via the shear along the $\pm[\bar{1}1\bar{1}]_\alpha$ direction. The transition to the $\epsilon$ phase is completed by following shuffle movements, which are alternative displacements of

adjacent $(110)_\alpha$ planes along the $\pm[101]_\alpha \parallel [12\bar{3}0]_\epsilon$ direction. Each configuration generates a set of conjugate planes of $(\bar{1}01)_\alpha \parallel (0001)_\epsilon$ and $(1\bar{2}1)_\alpha \parallel (21\bar{3}0)_\epsilon$ or $(121)_\alpha \parallel (\bar{1}100)_\epsilon$. Therefore, the Burgers model allows two directions of shear deformation for one $\{110\}_\alpha$ plane. Consequently, a total of 12 $\epsilon$ variants can appear via the transition because there are six equivalent $\{110\}_\alpha$ planes in the bcc structure.

Table I summarizes the 12 variants introduced by the Burgers model. The 12 variants are categorized according to the shear direction and conjugate $\{110\}_\alpha$ planes with $(0001)_\epsilon$. Table I also shows the identifiers used in this paper to distinguish each variant. Two groups of $\{110\}_\alpha$ planes can be defined by the angles between the directions of the plane normal and the main compression $[111]_\alpha$ axis: $90°$ and $35.26°$. This study identifies the former $\{110\}_\alpha$ planes as type $A$ (orange-colored planes of the polyhedron in the inset of Fig. 1) and the latter as type $B$ (blue colored). The letters and numerals following the indicators $A/B$ stand for the conjugate $\{110\}_\alpha$ planes (a)–(f) and the direction of shear deformation (1–4), respectively. Different types and colors of symbols are also used to distinguish the simulated XRD patterns of each variant and their shear directions for clarity.

Figures 1(f) and 1(g) show another transition model reported by Basset and Huang [15] and Wang and Ingalls [11]. This paper calls this model the uniaxial compression model. Unlike the Burgers model, this model does not rotate the crystal orientation of the hcp phase with respect to $[010]_\alpha$ that is $[010]_\alpha \parallel [\bar{1}010]_\epsilon$. The hcp structure emerges from the bcc structure by: (i) compression along the $[010]_\alpha$ direction and elongation along the $[101]_\alpha$ direction to form the $(0001)_\epsilon$ plane, and (ii) shuffle movements of the alternative $(\bar{1}01)_\alpha$ layers in the $\pm[101]_\alpha$ direction. The transition develops epitaxially with the orientational relationship $(010)_\alpha \parallel (\bar{1}010)_\epsilon$ as pointed out elsewhere [15].

## III. EXPERIMENTAL PROCEDURES

Single-crystalline iron plates with a (111) surface (Crystal Base Co., LTD) were prepared. These plates were cut using an electronic discharge machine or a razor blade after

TABLE II. Summary of the experimental setups for this paper. The sizes of the diamond anvils, iron samples, and thicknesses of SUS304 gaskets are tabulated for each run.

| Run | Beam size ($\mu$m) | Pressure medium | Culet[a] (mm) | Sample ($\mu$m$^2$) | Gasket ($\mu$m) | $\Delta\omega$ ($\circ$) |
|---|---|---|---|---|---|---|
| I | $20^{\phi}$ | He | $0.45^{\phi}$ | $25^t \times 65^{\phi}$ | $60^t$ | $28°$ |
| II | $3^{\phi}$ | He | $0.60^{\phi}$ | $25^t \times 90^{\phi}$ | $72^t$ | $15°$ |
| III | $3^{\phi}$ | ME[b] | $0.45^{\phi}$ | $30^t \times 95^{\phi}$ | $71^t$ | $15°$ |

[a]Each anvil height is 2.0 mm.
[b]Methanol:ethanol = 4:1 solution.

polishing the surface parallel to the (111) plane to achieve an approximate plate thickness of 25–30 $\mu$m. One of the iron plates was mirror polished for observation of the sample surface using a differential interference contrast (DIC) image. A small disk of the sample was loaded into the hole of the stainless steel gasket (SUS304) with a helium pressure medium or ME (4:1 ratio) solution. Diamond-anvil cells (DACs) were used as the pressure apparatus. No heat treatment was performed before sample loading. The setup of the diamond anvil cell for each run is summarized in Table II together with the setup for the XRD measurements.

XRD patterns were measured on BL10XU of SPring-8 at room temperature with an x-ray wavelength of $\lambda = 0.41\,310(7)$ Å. Angular dispersive XRD patterns were recorded on the imaging plate at each pressure as shown in Fig. 2. During the exposure, the DAC rotated around the vertical axis $\omega$ within a range of $\Delta\omega = 28°$ for run I. The rotation was performed to collect as many Bragg spots from the sample as possible. As for runs II and III, the $\omega$ range reduced to $\Delta\omega = 15°$ because of the narrower windows of the DACs dedicated to the compatible measurements of XRD and DIC images. The $\omega$ axis was set approximately parallel to $[01\bar{1}]_\alpha$, and the incident x-ray beams were oriented on the $[111]_\alpha$ axis when the $\omega$ axis rotates $\approx +3.7°$ for run I and $\omega \approx +1.5°$ for run II from the center of the rotation, i.e., $\omega = 0°$. The x-ray beams were cut to a size of 20 $\mu$m$\phi$ by using a
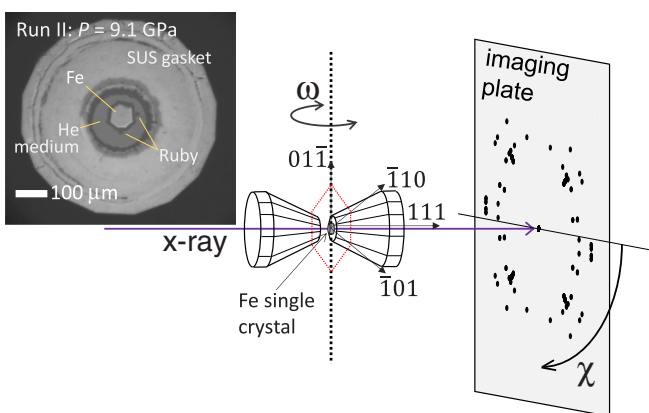


FIG. 2. Schematic of the setup for the x-ray diffraction experiments. The relationship between the crystal orientation, x rays, and the $\omega$-rotation axis is depicted. The inset shows a DIC photograph of the mirror-polished sample in the DAC. The iron crystal was the sample used for run II.

collimator for run I, whereas runs II and III used x-ray beams with $\leqslant 3$ $\mu$m$\phi$, focused by an array of aluminum refractive lenses [16,17]. Therefore, the well-focused beam used for runs II and III irradiated x rays on the focused position of the sample more easily than the beam of run I. The IPANALYZER and PDINDEXER software processed the XRD patterns [18]. An Olympus BX60 microscope with a long working distance (WD) objective lens ($\times 50$, WD = 11 mm) aided in recording the DIC images of the texture structure on the surface at each pressure.

The pressure in the sample room was measured by the conventional ruby fluorescence method. As shown in the inset of Fig. 2, two ruby balls were attached to the sample. No difference was confirmed in the calculated pressure values between the two rubies up to the maximum pressure of this paper. However, it is noted that the pressure value has an error bar less than 0.2 GPa if we take into account the uncertainty of the pressure gauges [19]. We calculated the pressure value by using a recent pressure gauge [19]. The applied pressure was controlled manually by using a gear box. This gear box allowed us precise pressure control with resolution less than 0.1 GPa. Therefore, we carefully adjusted the pressure and waited until the pressure was stabilized. This procedure is necessary to exclude the deviation of the transition pressure due to the kinetic effects of pressure nonuniformity.

## IV. RESULTS AND DISCUSSION

### A. Run I: Transition process under the quasihydrostatic condition

#### 1. X-ray diffraction patterns of a Fe single crystal and onset and offset pressures of the transition

Figures 3(a)–3(d) depict two-dimensional images of the XRD pattern for the $\alpha$-$\epsilon$ transition together with patterns of the $\alpha$ phase in the compression and decompression processes. Figure 4 summarizes the pressure dependence of the lattice constants, intensity of the selected reflections, and their widths. Sixfold symmetry with respect to the $[111]_\alpha$ direction is clearly recognized in the diffraction pattern of the $\alpha$ phase [Fig. 3(a)]. Sharp $110_\alpha$ Bragg spots were observed with a high signal-to-noise (S/N) ratio (S/N approximately 4000), even though the annealing treatment was not performed. Because quasihydrostatic conditions were maintained by the helium pressure medium, the Bragg spots remained sharp until $P$ reached the onset pressure $P_{\text{on}}^{\alpha \to \epsilon} = 14.0$ GPa. New spots identified as the $\epsilon$ phase appear above $P_{\text{on}}^{\alpha \to \epsilon}$, and the spots of the remaining $\alpha$ phase become broad. More than half ($\geqslant 60\%$) of the $\alpha$-phase abundance abruptly transforms to the $\epsilon$ phase if the intensity of the $112_\alpha$ reflection is assumed to be proportional to the phase abundance. Above $P_{\text{on}}^{\alpha \to \epsilon}$, the $\alpha$-phase abundance gradually decreases, whereas the $\epsilon$ phase increases with increasing $P$. Therefore, the $\alpha \to \epsilon$ transition proceeds in two steps: the sharp transition to the $\epsilon$ phase and the gradual decrease in the remaining $\alpha$-phase abundance. The two-step transition is similar to previous experiments using a helium pressure medium [12,13]. The intensities from the $\epsilon$ phase do not change, and those from the $\alpha$ phase are mostly zero above the offset pressure $P_{\text{off}}^{\alpha \to \epsilon} \sim 17$ GPa, indicating that the $\alpha \to \epsilon$ transition finishes at $P_{\text{off}}^{\alpha \to \epsilon}$. The onset $P_{\text{on}}^{\alpha \to \epsilon}$ is nearly identical
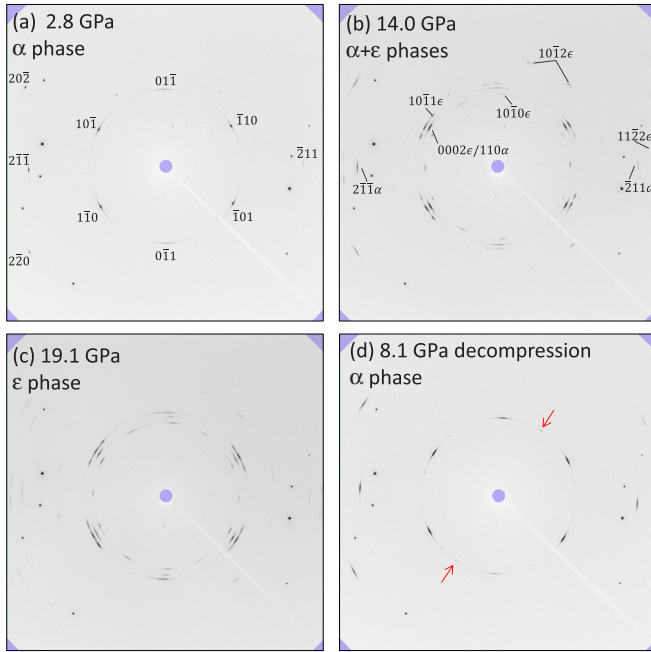
FIG. 3. X-ray diffraction patterns of iron at selected pressures of run I. Unindexed spots mostly originate from Bragg diffraction of the ruby balls and diamond anvils. Weak spots due to the contamination of higher harmonics of the incident x ray are also observed. The red arrows in panel (d) indicate spots from the newly appeared $\alpha$-phase variants after the decompression process.



FIG. 4. (a)–(c) Pressure dependences of lattice constants, (d) cell volume of $\alpha$ and $\epsilon$ phases, (e) and (f) peak width, and (g) and (h) intensity of the selected reflections. Closed (open) symbols are used for the compression (decompression) processes. The data for the $\alpha$ and $\epsilon$ phases are plotted by black and red colored symbols, respectively.

to the onset pressure (14.2 GPa) for previous experiments of compression along $[100]_\alpha$ [13]. Thus, the onset pressure does not change depending on the crystal orientation of the sample in the case of static compressions within the error bar of pressure (0.2 GPa), which is similar to the orientation-independent behavior under shock compressions [20].

In the decompression process, the $\alpha$ phase reappears from $P_{\mathrm{on}}^{\epsilon\to\alpha} \sim 10.9$ GPa, and the entire sample recovers the $\alpha$ phase at $P_{\mathrm{off}}^{\epsilon\to\alpha} \sim 8.5$ GPa. The pressure values of $P_{\mathrm{on}}^{\epsilon\to\alpha}$ and $P_{\mathrm{off}}^{\epsilon\to\alpha}$ are close to those of previous reports [13,21,22]. Therefore, the reverse transformation to the $\alpha$ phase seems also orientation independent. It is noted that the positions of the Bragg spots rotate slightly in the clockwise direction around the beam direction accompanied with the progress of the transitions. The degree of rotation is $\chi \sim 3°$ for $\alpha \to \epsilon$ and $\chi \sim 1.5°$ for the $\epsilon \to \alpha$ transition where the parameter $\chi$ is the angle along the circumference on the image in the clockwise direction (see Fig. 2).

Earlier works of compression with polycrystalline samples reported anomalously large values of the $c/a$ ratio at the onset pressure, e.g., $c/a \sim 1.64$ [15] and $\sim 1.66$ [11]. The $c/a$ values dropped rapidly with increasing pressure. This anomaly is regarded as evidence for large elastic distortions due to the epitaxial growth at the interface $(010)_\alpha \parallel (\bar{1}010)_\epsilon$ [15]. As shown in Fig. 4(c), this behavior is not observed in this paper as well as the previous report of quasihydrostatic compression along the $[100]_\alpha$ direction [13,23]: The $c/a$ ratio is mostly unchanged with increasing pressure and shows a slight decrease from 1.606 to 1.605 near $P_{\mathrm{off}}^{\alpha\to\epsilon}$. The constant $c/a$ ratio indicates that strains inside both phases and at their

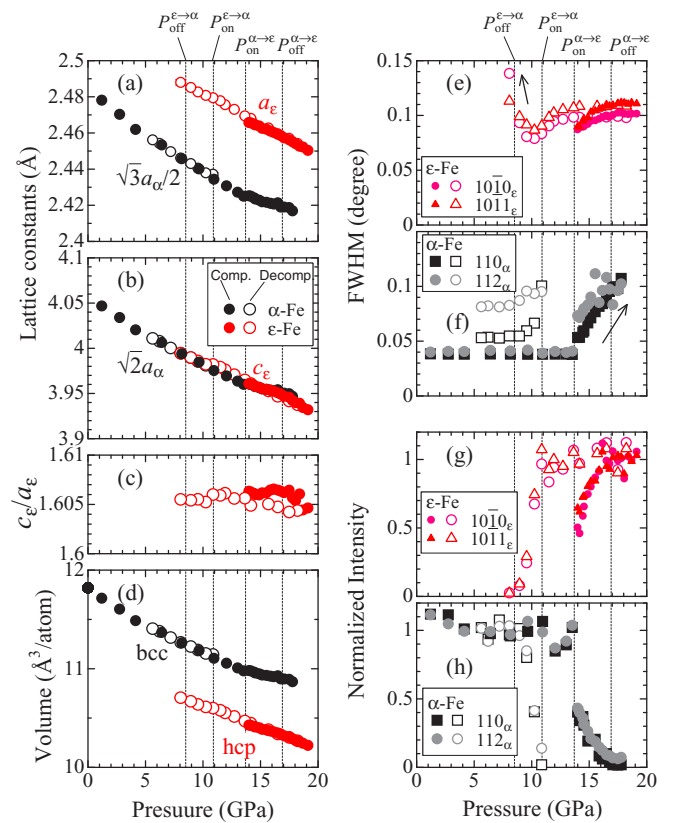interface are effectively released during the transition by the stabilized field of compression. The remaining strain probably concentrates in the minor phase; the strain accommodated in the minor phase increases the width of the Bragg peak when the abundance of the minor $\alpha$ or $\epsilon$ phase is significantly suppressed near the offset pressure. This behavior is observed at the full width at half maxima (FWHMs) of the parent $\alpha$ phase in the $\alpha \to \epsilon$ transition and the $\epsilon$-martensite phase in the reverse $\epsilon \to \alpha$ transition as shown in Figs. 4(e) and 4(f). To highlight these phenomena, the increases in the FWHM near the offset pressure are indicated by arrows in Figs. 4(e) and 4(f).

### 2. Analysis of variant selection: α-ε transition

Comparing the position of the Bragg spots between the experimental observations and the simulation based on the Burgers model, we determine the variant selection at the $\alpha$-$\epsilon$ transition. In order to simulate the XRD patterns of the 12 $\epsilon$-phase variants, maps of the reciprocal points were drawn for each variant in the three-dimensional reciprocal space. Then, we examined how the reciprocal points were superimposed on the surface of the Ewald sphere by rotation along the $[01\bar{1}]_\alpha$ axis. We note that all Bragg spots shaded by the window of DAC were excluded from the simulation. The shading
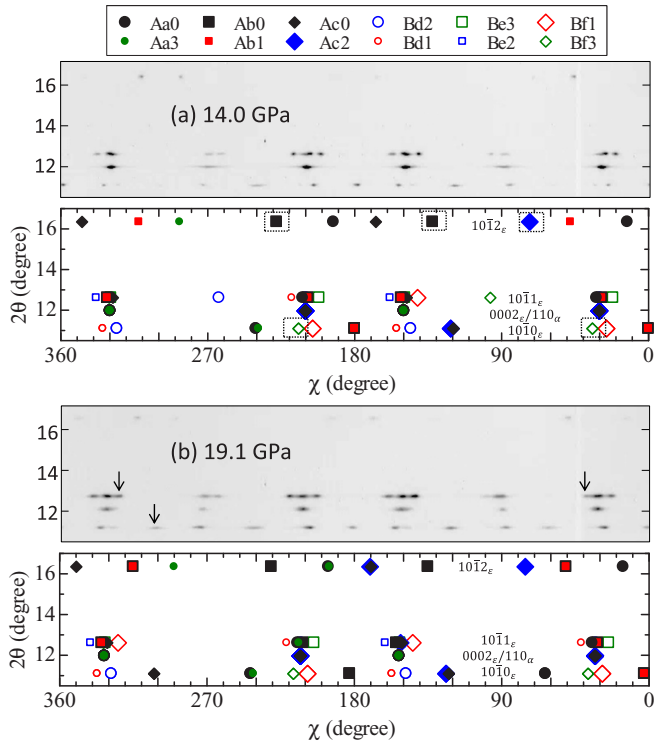
FIG. 5. X-ray diffraction patterns of run I and simulations based on the Burgers model at (a) $P_{on}^{\alpha \to \epsilon}$ and (b) a pressure above $P_{off}^{\alpha \to \epsilon}$. All patterns are shown as unrolled patterns with azimuth $\chi$ and $2\theta$ axes. Each symbol corresponds to the Bragg spots from the $\epsilon$ variant as shown in the legend above. The simulations at the onset and offset pressures are calculated using different $\omega$ ranges [$-10.3° \leqslant \omega \leqslant +17.7°$ for panels (a) and $-14° \leqslant \omega \leqslant +14°$ for panel (b)]. The symbols marked by dotted squares represent the absent or very weak Bragg spots in the experimental XRD patterns. The downward arrows indicate newly appearing Bragg spots during the transition.

effect occurs even within the small $2\theta$ less than $15°$ due to the simultaneous rotation of the DAC with the sample. The simulation was performed by using the commercial software MS-EXCEL.

Figure 5 depicts the experimental and simulated XRD patterns in the space of the $\chi$ and $2\theta$ axes at the onset and offset pressures. These XRD patterns are fairly reproduced by the Burgers model except for the spots near the vertical direction: $\chi = 90°$ and $\chi = 270°$. In principle, the simulation ignores the broadening of the reciprocal points, thus, the Bragg law is hardly satisfied for the reciprocal points near the $\omega$ axis.

As shown in Fig. 5, all of 12 variants do not appear simultaneously at $P_{on}^{\alpha \to \epsilon}$. The observed variant can be categorized by the direction of the shear deformation as tabulated in Table I. As marked by the dotted squares in Fig. 5, the spots from the three variants, Ab0, Ac2, and Bf3, do not appear or give only faint images in the experimental patterns. Three variants, Ab1, Bd1, and Bf1, induced by the same shear deformation along $\pm[\bar{1}11]_{\alpha}$, appear as the major components, and two variants, Aa3 and Be3 by the $\pm[11\bar{1}]_{\alpha}$ shear are the second major components. Alternatively, weak and distorted spots indicate that the variants Bd2 and Be2, by the $\pm[1\bar{1}1]_{\alpha}$ shear, and

variants Aa0 and Ac0 by $\pm[111]_{\alpha}$ shear, are categorized as the minor components.

The determined variant selection offers a transition process via compression along the $[111]_{\alpha}$ direction: (i) a variant emerges together with one or two twined variant(s) induced by the same shear deformation [24]. The twin originates from the cooperative variant selection to relax the strain and minimize the energy at the interface between the $\alpha$ and $\epsilon$ phases [25], and (ii) the shear deformation parallel to $\pm[111]$ compression axis is a minor component. The major components of shear have a finite angle of $70.53°$ with the compression axis. All three variants, Ab1, Bd1, and Bf1, appear from the onset pressure as a result of the $[\bar{1}11]_{\alpha}$ shear distribution.

As indicated by the arrows in Fig. 5(b), new Bragg spots emerge and increase their intensity with increasing pressure to $P_{off}^{\alpha \to \epsilon}$. Our simulation based on the $\omega$ range of $\omega = -10.3°$ to $+17.7°$ does not predict the $\chi$ positions of new spots. When we modify the rotation range to $\omega = -14°$ to $+14°$, the $\chi$ distribution of the spots is reproduced. This modification suggests that the sample rotates slightly around the $\omega$ axis, which is probably due to the intrinsic transition process or that the sample moved slightly by touching the diamond anvil. The new peaks are identified as the Ac0, Bd1, and Bf1 variants that have already been assigned at $P_{on}^{\alpha \to \epsilon}$. Therefore, new variants do not appear up to the offset pressure, and the initial set of $\epsilon$ phase variants increase their abundances by eliminating the residual $\alpha$ phase. Thus, the transition proceeds without generating new variants.

### B. Run II: Variant distribution under the quasihydrostatic condition

The results of run I demonstrate the high reliability of the simulated XRD pattern based on the Burgers model. However, clear variant selection has not been observed because the size of the x-ray beam was large ($\sim$20 $\mu m\phi$) as compared to the size of the variants and likely probed the average distribution of the variants. Here, run II has been conducted to investigate the relationship between the variant selection and texture structure by using XRD with a well-focused beam ($\sim$3 $\mu m\phi$) and the DIC images. Figure 6 depicts two-dimensional images of the x-ray diffraction patterns (a)–(f) and DIC images (g)–(j) observed in the $\alpha$-$\epsilon$ transition of the mirror-polished sample. The Bragg spots of $110_{\alpha}$ remain sharp until the pressure reaches the onset pressure $P_{on}^{\alpha \to \epsilon} = 14.3$ GPa. The onset pressure is $\sim$0.3 and $\sim$0.1 GPa higher than $P_{on}^{\alpha \to \epsilon}$ of run I and the previous experiment of compression along $[100]_{\alpha}$, respectively [13].

The mirror surface of the sample is preserved at pressures below $P_{on}^{\alpha \to \epsilon}$, which also ensures quasihydrostatic conditions using the He pressure medium. As new spots of $\epsilon$ phases appear above $P_{on}^{\alpha \to \epsilon}$, textured structures simultaneously emerge on the mirror-polished surface [see Fig. 6(i)]. The undulations of the texture structure are approximately oriented along the directions of $[\bar{1}01]_{\alpha}$, $[0\bar{1}1]_{\alpha}$, and $[\bar{1}10]_{\alpha}$. The texture structure of the sample remains unchanged above $P_{off}^{\alpha \to \epsilon}$, which is located between 17.0 and 18.9 GPa.

The texture structure is characterized by two areas, referred to as $X$ and $Y$, that exhibit a different distribution of
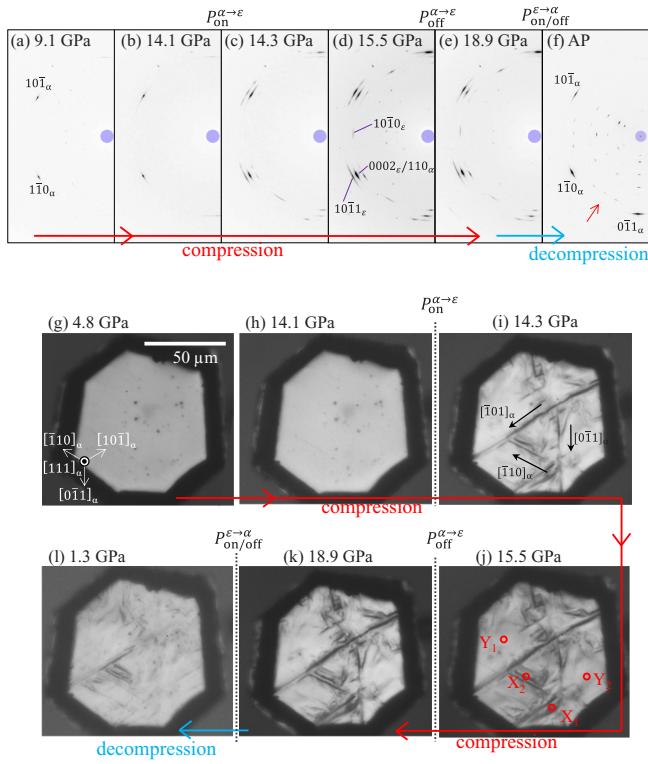
FIG. 6. Results of run II. Upper panels (a)–(f) show x-ray diffraction patterns measured at the center of the surface-polished sample. Unindexed spots mostly originate from Bragg diffraction form the ruby balls and diamond anvils. Weak spots due to the contamination of higher harmonics of the incident x ray are also observed. In panel (f), the spots originating from the higher harmonics are enhanced and distributed radially around the center. Lower panels (g)–(j) show DIC images of the sample surface taken during the XRD measurements. The red small circles labeled as $X_1$, $X_2$, $Y_1$, and $Y_2$ indicate the positions of the characteristic structure where the position-dependent XRD patterns were measured.



FIG. 7. Pressure dependence of x-ray diffraction patterns measured at the characteristic areas $X$ and $Y$. Top panel displays a simulated diffraction pattern based on the Burgers model. Each pattern is shown by the unrolled image with the axes of azimuth $\chi$ and $2\theta$ angles. The color of the circles corresponds to the assignment of the variants tabulated in Table I. Circles with solid and dotted lines in the experimental XRD patterns represent the spots of $A$-type and $B$-type variants, respectively. Note that only the selected spots are marked by the circles for the sake of simplicity.

undulations: $X$ is the region where the linear undulation is oriented along the three characteristic $\langle 110 \rangle_\alpha$ directions, and $Y$ corresponds to the flat regions without undulations as shown in Fig. 6(j). Figure 7 shows the typical XRD patterns measured at the areas $X_1$, $X_2$, $Y_1$, and $Y_2$ together with the simulated XRD pattern. Diffraction patterns of run II show a smaller number of Bragg spots than those of run I because of the narrow range of $\omega$ for run II as tabulated in Table II. However, the reproduction of the run II patterns by the Burgers model is as good as run I.

The XRD patterns of the $Y$ regions differ significantly from those in the $X$ regions: The $Y$ regions exhibit a reduced number of Bragg spots as compared to the $X$ regions, and the main spots are classified as type-$A$ variants and the minor spots as type-$B$ variants. The minor spots vanish, and only spots from type-$A$ variants remain at pressures above $P_{\mathrm{off}}^{\alpha \to \epsilon}$: 18.9 GPa. Interestingly, the remaining variants of type $A$ are identified as Aa3, Ab1, and Ac2 which emerge via the shear directions not parallel to $[111]_\alpha$, that is $[11\bar{1}]_\alpha$, $[\bar{1}11]_\alpha$, and $[1\bar{1}1]_\alpha$. The absence of $[111]_\alpha$ shear deformation is consistent with a flat surface without undulation. Because the shear directions of the three variants have threefold symmetry with
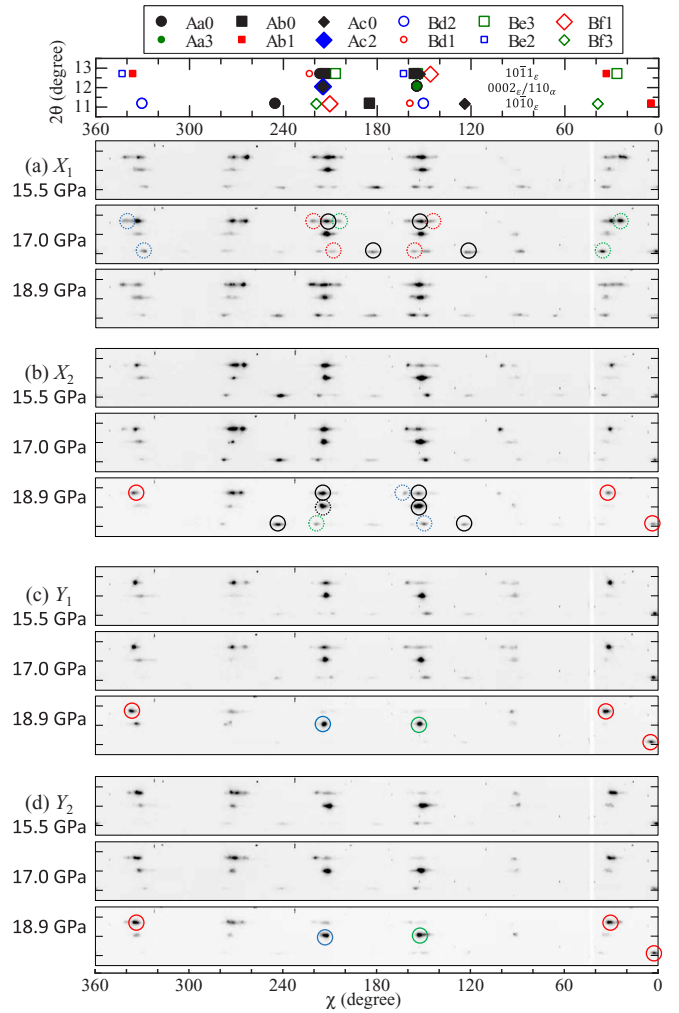
respect to the $[111]_\alpha$ direction, the lattice strain due to each shear deformation is canceled by stacking these three variants alternatively along the $[111]_\alpha$ direction. This variant selection is regarded as a cooperative emergence of variants as well as the twin [26]. Hence, the cancellation mechanism of the lattice strain results in the remaining flat surface after the transition. It should also be noted that the flat regions consist of only three variants, indicating that the number of variants can be reduced if the flat region area is enlarged.

$X_1$ and $X_2$ regions, where complicated texture structures and undulations are observed, exhibit XRD patterns similar to those of run I. The XRD patterns are reproduced by the variant distribution covering both types $A$ and $B$. The $A$-type twined variants introduced by the same $[111]_\alpha$ shear (i.e., Aa0, Ab0, and Ac0) exist in the $X$ regions. These variants are identified by the $10\bar{1}0_\epsilon$ Bragg spots at $\chi = 245°$, $185°$,

and 124°, respectively, whereas they are absent in the patterns of the $Y$ region. Because the $[111]_\alpha$ shear corresponds to the deformation to lift the atomic plane to the perpendicular direction of the (111) sample surface, the undulation structure likely originates from these variants with $[111]_\alpha$ shear. In the case of the $X_2$ region, the $[111]_\alpha$ shear movement is introduced by the dominant emergence of the Aa0 variant. Then, this shear movement of Aa0 creates boundaries between the $\alpha$ and $\epsilon$ phases along $[\bar{1}01]_\alpha$, which is parallel to the direction of undulations observed in the $X_2$ region. The interpretation of the texture structure around region $X_1$ is rather complicated. Twined Ab0 and Ac0 variants appear at 17.0 GPa, however, Aa0 becomes dominant at 18.9 GPa. Ab0 and Ac0 create boundaries along $[0\bar{1}1]_\alpha$ and $[10\bar{1}]_\alpha$, which is also parallel to the directions of the undulations in the $X_1$ region where the main undulation is oriented along $[10\bar{1}]_\alpha$ and broad contrast arises along $[0\bar{1}1]_\alpha$.

### C. Run III: Variant distribution under the nonhydrostatic condition

It is nontrivial to compare the results of quasihydrostatic compression with those under nonhydrostatic compression along the $[111]_\alpha$ direction. A new iron (111)$_\alpha$ plate was prepared and compressed with the ME solution. The nonhydrostatic compression resulted in different XRD patterns and surface undulations. Figure 8 shows that the surface undulations start to appear at pressures after the solidification of the ME medium (∼10 GPa) [27] and gradually increase with increasing pressure even before the $\alpha$-$\epsilon$ transition. The undulation emerges due to the strain induced by uniaxial compression along $[111]_\alpha$. The presence of the uniaxial strain is recognized in the DIC images where the sample surface area becomes wider than the initial condition. The surface undulation increases significantly at 14.6 GPa, which is a pressure above $P_{on}^{\alpha\to\epsilon}$. However, the undulation does not change drastically above $P_{on}^{\alpha\to\epsilon}$. As shown in Fig. 8, surface undulations lie along various orientations, and the relationship between the crystal orientation and the undulation is hardly recognized in contrast to their clear relationship under hydrostatic compression [28]. The density of undulation is mostly uniform but slightly denser in the lower part of the DIC images.

Figure 8 demonstrates that the diffraction patterns of run III cannot be reproduced by the Burgers model. The Burgers model with compression along $[111]_\alpha$ is characterized by splitting of the $10\bar{1}0_\epsilon$ and $10\bar{1}1_\epsilon$ Bragg reflections with respect to the $\chi$ angles of the $0002_\epsilon$ spot (see Figs. 5 and 7). The splitting originates from the Burgers model that allows two variants for each of the six $\{110\}_\alpha$ planes, for example, Aa0 and Aa3. However, run III exhibits that $10\bar{1}0_\epsilon$ Bragg spots do not split and appear at a slightly higher or lower $\chi$ angle for the $10\bar{1}1_\epsilon$ reflections. As shown in Fig. 8, the uniaxial compression model provides more suitable patterns to reproduce the experimental XRD pattern, although there are some inconsistencies between the experimental and the simulated XRD patterns. This result indicates that the shear deformation is not a trigger for the transition, whereas the uniaxial deformations along the $\langle 100 \rangle_\alpha$ and $\langle 110 \rangle_\alpha$ directions seem to have dominated to the emergence of the $\epsilon$-phase variants. Figure 9(a) shows that $A$-type variants (Aa$_u$, Ab$_u$, and Ac$_u$)
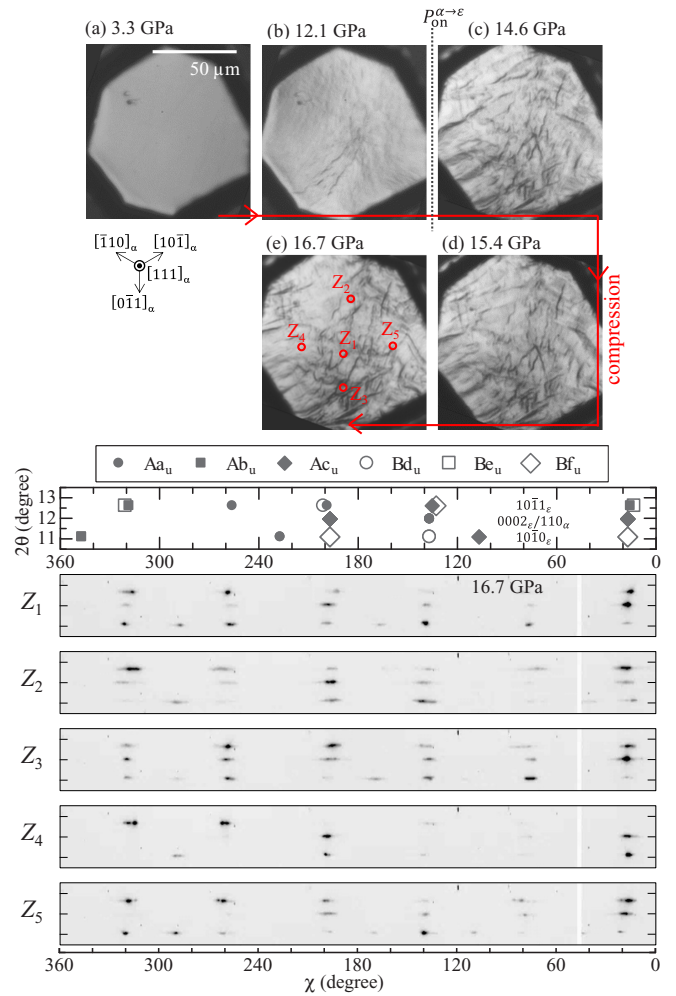


FIG. 8. Results of run III. Top: DIC images under nonhydrostatic conditions using ME pressure medium at selected pressures. Middle: A simulated diffraction pattern based on the uniaxial compression model. Bottom: Unrolled x-ray diffraction patterns of 16.7 GPa at positions of $Z_1$–$Z_5$.
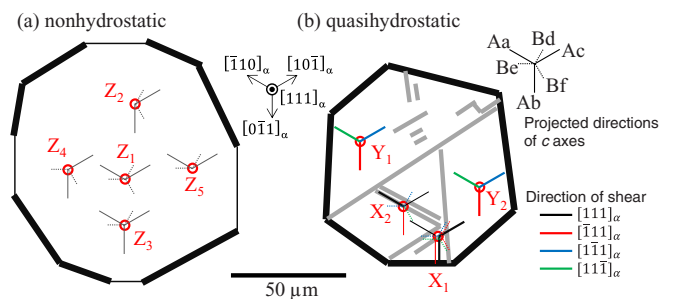


FIG. 9. Illustrations of $c$-axis distribution on the sample surface determined by XRD patterns for (a) nonhydrostatic and (b) quasihydrostatic conditions. The long-solid lines represent the $c$ axes of $A$-type variants that are oriented parallel to the sample surface, and the short-dotted lines denote the projected $c$ axes of the $B$-type variants (see the right top legend). The direction of shear (0–4) for the Burgers model is distinguished by the color of the lines as shown in the right bottom legend. The $c$ axis of the dominant variants is represented by thick lines.

and $B$-type variants ($Bd_u$, $Be_u$, and $Bf_u$) equivalently appear to be independent in the five positions of the sample ($Z_1$–$Z_5$), even though the different orientational relationships between the deformation and the compression axis exist for $A$-type and $B$-type variants.

It is concluded that the compressions along the $[111]_\alpha$ orientation exhibited strong variant selections only in the case of the quasihydrostatic condition. Furthermore, different variant selections were observed in the characteristic regions of texture structure: regions with undulations ($X$) and flat areas without undulations ($Y$). The determined variant distribution is illustrated in Fig. 9(b). Region $Y$ consists of only three variants whose shear deformations have a threefold symmetry to compensate for the strain due to the transition. All $c$ axes of the $\epsilon$ variants align parallel to the $(111)_\alpha$ sample surfaces with threefold symmetry as illustrated in Fig. 9 where the directions of the $c$ axes are depicted. Therefore, the variant distribution in region $Y$ can be used to investigate the anisotropy of physical properties in $\epsilon$ iron. Conversely, the variant distribution in region $X$ is more complicated because the $c$ axes of variants do not orient solely to the direction of undulation, but also align in other directions with the components of the surface normal. Because region $Y$ is surrounded by undulations in region $X$, it is important to investigate how to enlarge the area of $Y$ regions by reducing the number of undulations. One sides of the undulations terminated at the corner of the sample so that strains accommodated at the corner likely worked as nucleation which generated the undulations when the $\alpha$-$\epsilon$ transition occurred. A disklike sample without corners may be valuable to examine the reduction in the number of undulations.

## D. The $\epsilon$-$\alpha$ reverse transition under the quasihydrostatic condition

In the decompression process under the quasihydrostatic condition, the sample recovers the original diffraction pattern of the $\alpha$ phase as shown in Fig. 3(d) for run I and Fig. 6(f) for run II. The $110_\alpha$ spots reappear near the original $\chi$ positions, indicating that the $\alpha$-$\epsilon$ martensitic transition is mostly reversible. However, weak intensities of the new $110_\alpha$ spots are also observed at different $\chi$ positions as indicated by the arrows. Run I shows weak Bragg spots at $\chi \sim 123°$ and $\chi \sim 303°$ as shown in Fig. 10 where the intensity of $110_\alpha$ spots is plotted on a logarithmic scale as a function of $\chi$. The intensity of these peaks is approximately 65 times weaker than that of the peaks at the original $\chi$ positions. Very weak peaks are also observed around the original $110_\alpha$ spots, but the intensity is approximately 250 times smaller than the original.

There are six pathways allowed for the reverse transformation from the hcp structure to bcc; three directions for the shuffle movement due to the threefold symmetry of the hcp structure and two directions for the shear deformation via the mirror symmetry of the crystal structure after shuffle movements (see Fig. 10). Accordingly, weak new peaks originate from one minor variant Ac0. The Ac0 variant emerges via the $\pm[111]_\alpha$ shear deformation and $\pm[101]_\alpha$ shuffle movements from the parent $\alpha$ phase. Figure 10 depicts that the reverse transition from Ac0 does not trace the original shuffle movements but takes one of the two other directions of the
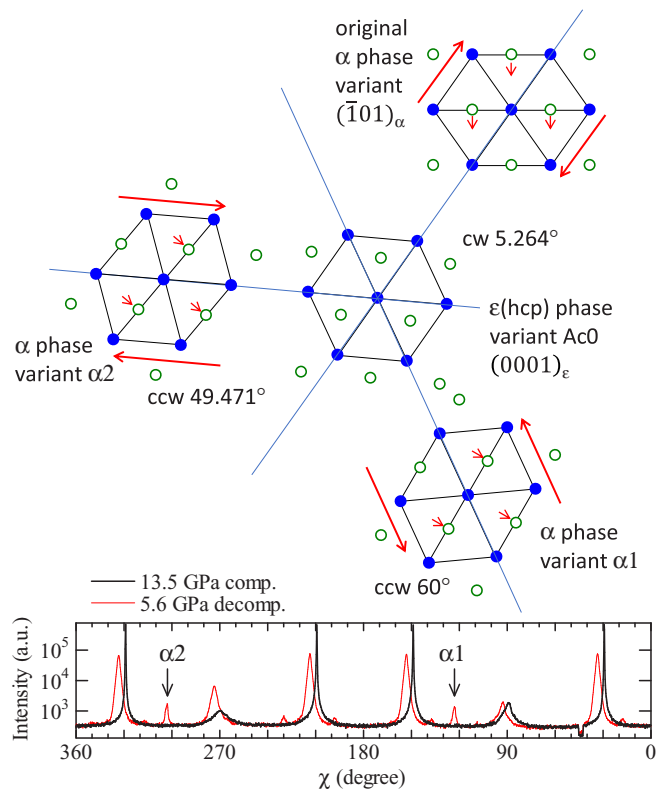


FIG. 10. The upper part shows a schematic of the predicted atomic displacements for the $\alpha \to \epsilon \to \alpha$ phase transition via the Ac0 variant. The schematic represents an hcp structure that allows two paths to return to the bcc phase for each shuffle movement. The lower part shows comparison of the $110_\alpha$ diffraction as a function of angle $\chi$ before the $\alpha \to \epsilon$ transition and after the $\epsilon \to \alpha$ transition. The XRD data were taken from run I. The two arrows indicate the new peak emerging after the $\epsilon \to \alpha$ transition in the decompression process.

shuffle. Consequently, the shear deformation also works in different directions from the original. The two new spots are identified as $\alpha 1$ and $\alpha 2$ variants and generated via the same shuffle and different shear deformations. The $\alpha 1$ and $\alpha 2$ variants have crystal orientations in which the original $\alpha$ phase rotates 60° and 49.47° around the $[\bar{1}01]_\alpha \parallel [0001]_\epsilon$ axis in the anticlockwise direction. Note that the very minor irreversible components near the original $110_\alpha$ spots are attributed to the reverse transition from the $B$-type $\epsilon$-phase variants via different pathways.

The same decompression process of the XRD patterns are observed for run II. Intense Bragg spots from the original $\alpha$ phase, and weak spots are observed at the same positions in run I as indicated by the arrow in Fig. 6(f). Therefore, the weak spot could be assigned to the $\alpha 1$ variant, indicating that a small portion of the $\epsilon$-phase iron traces a different transition pathway from the original path. The DIC image in Fig. 6(l) shows that the surface undulations are significantly suppressed after the reverse transition to $\alpha$ phase. However, the sample is no longer mirror polished, and weak undulations remain on the surface. The weak Bragg spots assigned as $\alpha 1$ or $\alpha 2$ are observed mainly in the damaged areas near the $X_1$ and $X_2$ regions. In contrast, the regions near $Y_1$ and $Y_2$ provide

Bragg spots from the nonoriginal $\alpha$ phase with weaker or mostly zero intensities. Therefore, the irreversible transition dominantly occurs in the strain-accommodating areas near the undulation.

Our results demonstrate that most of the sample recover the original bcc structure by tracing the same pathways of shear and shuffle movements, which is similar to the previous results of the $100_\alpha$ sample under quasihydrostatic conditions [13]. The reversible transition is reminiscent of the mechanism of shape-memory alloys. However, the same mechanism is unexpected for the reconstructive martensitic transformation of iron because the parent bcc and the martensite hcp structure are not members of the same crystal family. According to the theoretical investigation by Bhattacharya *et al.* [29], a necessary condition for reversibility is that the symmetry groups of the parent and martensite phases be included in a common finite symmetry group. Therefore, it is speculated that the characteristic variant selections observed in the $X$ and $Y$ regions probably result in constraining the pathway of the reverse transition to the $\alpha$ phase. As discussed above, the cooperative deformation of shear and shuffle movements due to the strong variant selection not only reduces the strain in the sample, but also forces the tracing of the reverse pathway to the original $\alpha$ phase.

## V. CONCLUSIONS

The emergence of $\epsilon$-phase variants via the $\alpha$-$\epsilon$ martensitic transformation was investigated by XRD and DIC images of a single-crystal iron compressed along the $[111]_\alpha$ orientation under quasihydrostatic and nonhydrostatic conditions. A characteristic texture structure, accompanying the $\alpha$-$\epsilon$ transition, was observed by DIC observation. Although the Burgers model allows for the transformation to 12 variants of the $\epsilon$ phase from a single crystal of the bcc structure, the variant selection occurred depending on the regions of the texture structure in the case of quasihydrostatic compression. On the other hand, clear variant selection was not confirmed for the nonhydrostatic compression. For the decompression process to the parent $\alpha$ phase, the quasihydrostatic condition mostly recovered the initial crystal orientation of the bcc structure. The $\alpha$ phase, with different crystal orientations, emerged as a minor component in the distorted regions near the undulations. The reversibility of the transition indicates the cooperative emergence of variants via the $\alpha$-$\epsilon$ transition.

A single-crystalline $\epsilon$ phase was not synthesized, however, the number of variants was reduced by utilizing variant selections under quasihydrostatic compression along the $[111]_\alpha$ direction. Only three variants existed in the flat areas of the $Y$ region. In this area, the $c$ axis of the variant oriented parallel to the (111) sample surface, and the strong preferred orientation should be useful to investigate the anisotropy of various physical properties for the $\epsilon$ phase. However, the flat region was limited to a small area of less than $20 \times 20$ $\mu$m$^2$, which was surrounded by the undulations of the $X$ regions. The $X$ regions possessed a large number of variants whose $c$ axes aligned both parallel and nonparallel to the sample surface. Therefore, in order to enlarge the area of the flat region $Y$, it is necessary to investigate how the nucleation of undulations is introduced in the sample.

[1] D. Bancroft, E. L. Peterson, and S. Minshall, J. Appl. Phys. **27**, 291 (1956).

[2] K. Shimizu, T. Kimura, S. Furomoto, K. Takeda, K. Kontani, Y. Onuki, and K. Amaya, Nature (London) **412**, 316 (2001).

[3] D. Jaccard, A. Holmes, G. Behr, Y. Inada, and Y. Onuki, Phys. Lett. A **299**, 282 (2002).

[4] K. Glazyrin, L. V. Pourovskii, L. Dubrovinsky, O. Narygina, C. McCammon, B. Hewener, V. Schünemann, J. Wolny, K. Muffler, A. I. Chumakov, W. Crichton, M. Hanfland, V. B. Prakapenka, F. Tasnádi, M. Ekholm, M. Aichhorn, V. Vildosola, A. V. Ruban, M. I. Katsnelson, and I. A. Abrikosov, Phys. Rev. Lett. **110**, 117206 (2013).

[5] J. Verhoogen, Geophys. J. Int. **4**, 276 (1961).

[6] Q. Williams, Annu. Rev. Earth Planet. Sci. **46**, 47 (2018).

[7] K. Ohta, Y. Nishihara, Y. Sato, K. Hirose, T. Yagi, S. I. Kawaguchi, N. Hirao, and Y. Ohishi, Front. Earth Sci. **6**, 176 (2018).

[8] A. Monza, A. Meffre, F. Baudelet, J.-P. Rueff, M. d'Astuto, P. Munsch, S. Huotari, S. Lachaize, B. Chaudret, and A. Shukla, Phys. Rev. Lett. **106**, 247201 (2011).

[9] G. Steinle-Neumann, L. Stixrude, and R. E. Cohen, Proc. Natl. Acad. Sci. USA **101**, 33 (2004).

[10] W. Burgers, Physica (Amsterdam) **1**, 561 (1934).

[11] F. M. Wang and R. Ingalls, Phys. Rev. B **57**, 5647 (1998).

[12] N. Ishimatsu, Y. Sata, H. Maruyama, T. Watanuki, N. Kawamura, M. Mizumaki, T. Irifune, and H. Sumiya, Phys. Rev. B **90**, 014422 (2014).

[13] A. Dewaele, C. Denoual, S. Anzellini, F. Occelli, M. Mezouar, P. Cordier, S. Merkel, M. Véron, and E. Rausch, Phys. Rev. B **91**, 174105 (2015).

[14] C. S. Yadav, G. Seyfarth, P. Pedrazzini, H. Wilhelm, R. Černý, and D. Jaccard, Phys. Rev. B **88**, 054110 (2013).

[15] W. A. Basset and E. Huang, Science **238**, 780 (1987).

[16] Y. Ohishi, N. Hirao, N. Sata, K. Hirose, and M. Takata, High Press. Res. **28**, 163 (2008).

[17] N. Hirao, S. I. Kawaguchi, K. Hirose, K. Shimizu, E. Ohtani, and Y. Ohishi, Matter Rad. Extremes **5**, 018403 (2020).

[18] S. Yusuke, http://pmsl.planet.sci.kobe-u.ac.jp/~seto/?lang=en.

[19] A. Dewaele, M. Torrent, P. Loubeyre, and M. Mezouar, Phys. Rev. B **78**, 104102 (2008).

[20] X. Liu, T. Mashimo, N. Kawai, T. Sano, and X. Zhou, J. Appl. Phys. **124**, 215101 (2018).

[21] R. Taylor, M. Pasternak, and R. Jeanloz, J. Appl. Phys. **69**, 6126 (1991).

[22] N. V. Barge and R. Boehler, High Press. Res. **6**, 133 (1990).

[23] A. Dewaele and G. Garbarino, Appl. Phys. Lett. **111**, 021903 (2017).

[24] S. J. Wang, M. L. Sui, Y. T. Chen, Q. H. Lu, E. Ma, X. Y. Pei, Q. Z. Li, and H. B. Hu, Sci. Rep. **3**, 1086 (2013).

[25] V. V. Dremov, G. V. Ionov, F. A. Sapozhnikov, N. A. Smirnov, A. V. Karavaev, N. A. Vorobyova, and M. V. Ryzhkov, EPJ Web Conf. **94**, 04023 (2015).

[26] C. Houska, B. Averbach, and M. Cohen, Acta Metall. **8**, 81 (1960).

[27] N. Tateiwa and Y. Haga, Rev. Sci. Instrum. **80**, 123901 (2009).

[28] The observed undulation of run III does not change and remains after the decompression to the $\alpha$ phase, indicating that the strain between the variants is not released effectively.

[29] K. Bhattacharya, S. Conti, G. Zanzotto, and J. Zimmer, Nature (London) **428**, 55 (2004).